Selective inhibition of hsp90 paralogs: Structure and binding studies uncover the role of helix 1 in Grp94-selective ligand binding

Nanette L. S. Que,[1] Paul M. Seidler,[1] Wen J. Aw,[1] Gabriela Chiosis,[3] and Daniel T. Gewirth[1,2,*]

[1]Hauptman Woodward Medical Research Institute, Buffalo, NY 14203
[2]Department of Pharmacology and Therapeutics, Roswell Park Comprehensive Cancer Center Buffalo, NY 14263
[3]Chemical Biology Program, Memorial Sloan-Kettering Cancer Center, New York, NY 10065

Running Title: *Helix 1 determines access to Site 2 in Grp94 and Hsp90*

Keywords: Grp94, Hsp90, chaperone, PU-H36, PU-H71

To whom correspondence should be addressed:

Daniel T. Gewirth
Hauptman Woodward Medical Research Institute
700 Ellicott Street
Buffalo, NY 14203 USA
716-898-8635
E-mail: gewirth@hwi.buffalo.edu

Abstract

Grp94 is the endoplasmic reticulum paralog of the hsp90 family of chaperones, which have been targeted for therapeutic intervention via their highly conserved ATP binding sites. The design of paralog-selective inhibitors relies on understanding the structural elements that mediate each paralog's response to inhibitor binding. Here, we determined the structures of Grp94 and Hsp90 in complex with the Grp94-selective inhibitor PU-H36, and of Grp94 with the non-selective inhibitor PU-H71. In Grp94, the 8-aryl moiety of PU-H36 is inserted into Site 2, a conditionally available side pocket, but in Hsp90 it occupies Site 1, a non-selective side pocket that is accessible in all hsp90 paralogs. The structure of Grp94 in complex with the non-selective PU-H71 shows only Site 1 binding. Large conformational shifts involving helices 1, 4 and 5 of the N-terminal domain of Grp94 are associated with the engagement of the Site 2 pocket for ligand binding. To understand the origins of Site 2 pocket engagement, we tested the binding of Grp94-selective ligands to chimeric Grp94/Hsp90 constructs. These studies show that helix 1 of the Grp94 N-terminal domain is the discriminating element that allows for remodeling of the ATP binding pocket and exposure of the Site 2 selective pocket.

Introduction

The hsp90 chaperones are responsible for the regulation and maturation of a diverse set of proteins that contribute to the maintenance of cell homeostasis (1). The client proteins of these chaperones include soluble and membrane-bound proteins, transcription factors, regulatory and checkpoint kinases, growth factors, angiogenesis promoters, metalloproteinases, and telomerases (2-4). Inhibition or knock-downs of hsp90 chaperones lead to the loss of function of their clients. Because the clients of hsp90s include key players in cancer, neurodegenerative and inflammatory diseases, as well as in innate immunity, the chaperones have been targeted for therapeutic intervention (5-9).

Higher eukaryotes contain four hsp90 paralogs: Hsp90α and Hsp90β are found in the cytosol, Grp94 is in the endoplasmic reticulum (ER), and Trap-1 is mitochondrial. All four paralogs share a common organization, with an N-terminal ATP binding and regulatory domain (NTD), a middle domain, and a C-terminal dimerization domain. Chaperone function is driven by conformational changes associated with ATP binding to the NTD and its subsequent hydrolysis (3,5,10-12). Small molecule inhibitors that disrupt nucleotide binding to the NTD prevent the functionally relevant conformational changes and result in abortive client maturation. To date, hsp90 inhibitors have incorporated at least 19 different chemical scaffolds with a number of these inhibitors progressing into clinical trials (13,14). The first generation of these molecules were pan-hsp90 inhibitors that targeted all four paralogs, but with the failure to secure FDA approval for these drug candidates, subsequent efforts have evolved to include the targeting of individual paralogs (9,15-21).

The NTDs of the four paralogs exhibit sequence identities of 50% or more, and within the ATP binding cavity the identity exceeds 70%. This high sequence conservation has posed a challenge for selective inhibitor design. Detailed structural and biochemical studies, however, have led to a better understanding of differences in the paralog's ATP binding cavities. In particular, the ATP binding cavity includes three adjoining pockets, termed Site 1, Site 2, and Site 3. These pockets form pairwise compound binding sites with the central ATP binding cavity serving as the common partner. The ability of a ligand to access and stably bind to these compound sites in one paralog but not another contributes to binding selectivity.

Sites 1, 2 and 3 are occluded in the apo form of the protein, and access depends on the ability of the NTD to undergo conformational changes in the "lid" subdomain in response to ligand binding. The lid is comprised of helix 1, strand 1, helix 4, and helix 5 (H1, S1, H4, H5). Upon ATP binding, the lid of all hsp90s moves from the open to the closed conformation, covering the bound nucleotide and potentiating a closed dimer conformation. While this movement is common to all hsp90 paralogs, the movements to expose Sites 1, 2, or 3 in response to inhibitory ligands are paralog specific. Thus, for Site 1, which in Grp94 is lined by residues Leu104, Leu163, Phe199, Val209, Trp223, Ile247 (Hsp90 residues Leu48, Leu107, Phe138, Val148, Trp162, Val186), access involves the remodeling of the linker between helices 3 and 4 to reposition Leu163 (Hsp90 Leu107). This conformational shift occurs in all four paralogs, but in Grp94 it results in structural disorder along H4 that lowers the affinity for moieties targeting Site 1. Site 3 is outermost of the three pockets. The mouth of Site 3 is constricted by Thr171 and Gly196 (Thr115 and Gly135 in Hsp90). Access to Site 3 in Grp94 can be expanded by shifts in Thr171 and an unwinding of the start of H4. The equivalent motions have not been observed in Hsp90, however, and ligands that bind in Site 3 in Hsp90 exhibit energetically unfavorable conformations or interactions compared to the poses observed when binding to Site 3 in Grp94. (22-24).

While ligands can access Sites 1 and 3 in all paralogs, ligand access to Site 2 was first identified in Grp94 (15) and subsequently in fungal Hsp90s (25). Site 2, which in Grp94 is bordered by Leu104, Leu163, Phe199, Ala202, Phe203, Val209, Val211, Ile247, and Leu249, is more interior and hydrophobic than Sites 1 or 3. In the apo NTD of Grp94, Site 2 is blocked by the side chain of Phe199, and exposure of the site requires a 2.8 Å displacement of the backbone and a ~25 degree rotation of the side chain. In the densely packed interior of the NTD, this movement precipitates significant conformational adjustments to adjacent residues, first to Tyr200 and subsequently to H1, S1, H4, and H5. The Hsp90 equivalent of Phe199 is Phe138. Phe138 has not been observed to undergo similar displacements and expose Site 2 in mammalian Hsp90, forcing ligands with a preference for Site 2 into unfavorable conformations or alternate binding pockets (15,19). Thus, targeting Site 2 has been significant to the development of Grp94-selective inhibitors.

The reason for the differences in lid responses in the hsp90 paralogs is unknown. Here, we structurally characterize a Site 2 directed inhibitor bound to both Grp94 and Hsp90. We also determine the structure of a high affinity pan-hsp90 inhibitor bound to Grp94. We then

measured the binding of these ligands to chimeric Grp94 and Hsp90 proteins where elements of the lid subdomain were swapped. From this study, we identified H1 of Grp94 as the protein element that permits the internal amino acid movements that expose Site 2.

Results

PU-H36 binds to Grp94 with the 8-aryl group in Site 2.

PU-H36 is a purine-based inhibitor that differs from the previously studied PU-H54 in two ways: it contains a bulkier 2,4,6-trimethy 8-aryl moiety in place of the 2,4-dimethy group found on PU-H54, and the acetylenic pent-4-yn-1-yl tail is attached to the N9 position of the purine base instead of the N3 position in PU-H54 (**Figure 1**) (15). Together these changes correlate with a ~25-fold improvement in K_d, as well as a ~4-fold improvement in Grp94 selectivity over Hsp90 (**Table 1**). While modeling studies based on the Grp94:PU-H54 structure are consistent with the insertion of the PU-H36 8-aryl group into Site 2, the paucity of structures of PU-based compounds bound to Grp94 represents a gap in our understanding of the modes of binding available to these compounds. In particular, the structural constraints imposed by the narrow Site 2 channel, combined with the bulkier 8-aryl group of PU-H36 and the significant variation in binding affinity and Grp94-selectivity for different PU compounds led us to ask how PU-H36 is accommodated in the Grp94 binding pocket and how the Grp94 conformation adapts to the different ligand. To answer these questions, we co-crystallized the Grp94:PU-H36 complex and determined its structure at 2.8 Å resolution.

The crystallographic asymmetric unit consists of four Grp94:PU-H36 complexes with pseudo-equivalency between the A/B and C/D pairs, yielding two independent views of the complex. As seen in **Figure 2a**, the 8-aryl group of PU-H36 is inserted into Site 2, with the plane of the aryl moiety and the 2- and 4-methyl groups closely aligned with their equivalents in PU-H54 (PDB code 3o2f). The most notable difference in the two complexes is found in the conformation of H1 in the lid subdomain. In the PU-H36 complex, H1 shifts from its apo protein conformation and adopts either an angled “up” or “down” trajectory. However, it remains associated with the body of the N-terminal domain (**Figure 2b**). In the PU-H54 complex, by contrast, H1 is displaced outwards and loses its association with the body of the N-terminal domain (**Figure 2c**). These differences arise from changes in the placement of Tyr200 between the two complexes. In the PU-H36 complex, Tyr200 forms edge-on-pi interactions with Phe199, while in the PU-H54 complex the connection with Phe199 is lost and, compared to its position in the PU-H36 complex, Tyr200 is rotated outwards by an additional 77 degrees, forcing the further displacement of H1 from its position in the apo form of the protein (**Figure 2d**).

The reason for the differences in the placement of Tyr200 can be traced to the position of the attachment of the hydrophobic acetylenic tail on the two PU compounds (**Figure 1**). In PU-H36, the tail is attached to N9 of the purine ring. From there it adopts an extended conformation that projects into H3 while its underside is stabilized by extensive van der Waals interactions with the

face of Phe195 (**Figure 2a**). This moves H3 away from the ATP binding pocket beginning at Asn162. The resulting volume created by this displacement provides space for Tyr200 to maintain its association with Phe199 after Phe199 has moved and rotated to open up Site 2. By contrast, the tail in PU-H54 is attached at the N3 position. From this attachment point it cannot reach the hydrophobic interior face of H3. Instead, the N3-attached tail minimizes its solvent exposure by adopting a "scorpion tail"-like fold under the purine ring, foregoing extensive interactions with Phe195 in the process (**Figure 2e**). As a result, H3 does not move to expand the ATP binding pocket. This sterically blocks the potential Tyr200/Phe199 interaction, resulting in the larger movement of Tyr200. Thus, the larger repositioning of H1 is ultimately tied to the conformation of the acetylenic tail, which in turn is dictated by its site of attachment on the purine ring.

The structure of Grp94:PU-H36 also helps explain the improved binding of PU-H36 to Grp94 compared to PU-H54. A characteristic feature of all Grp94 complexes that expose Site 2 is the large rotation of Phe195 from its position sandwiched between H4 and H5 in the apo protein, into a position that shields the underside of the ATP binding pocket. The additional interactions between the PU-H36 tail and Phe195 suggest that these contribute positively to the improved binding of PU-H36 (Kd =2.6 μM) for Grp94 compared to PU-H54 (Kd = 69 μM), which lacks these interactions. The alkyl tail at N9 in this scaffold is thus more optimal for Grp94 binding as opposed to that at N3.

PU-H36 binds to Site 1 of Hsp90.

PU-H36 binds with higher affinity to Grp94 than to Hsp90, and also binds with higher affinity to Hsp90 than PU-H54 (**Figure 1, Table 1**). In Grp94, the 8-aryl group of PU-H36 inserts into Site 2 of the ATP binding pocket, and the N3-tail makes extensive interactions with Phe195 of H5. To visualize the placement of these elements when PU-H36 is bound to Hsp90, we crystallized the Hsp90:PU-H36 complex and solved the structure at 1.50 Å resolution. As seen in **Figure 3a**, the protein structure is identical to Hsp90:PU-H54 (PDB Code 3o01), with an RMSD of 0.088 Å for CA atoms. As with Hsp90-bound PU-H54, the 8-aryl group of PU-H36 is located in Site 1 of the binding pocket, rather than in the hydrophobic Site 2 as in Grp94 (**Figure 3b**) and this is likely to account for much of the energetic penalty these compounds incur in binding to Hsp90. In addition, the acetylenic tail, which is attached at the N3 of the purine ring in PU-H36, curves under the purine moiety in the "scorpion tail" conformation in a similar manner as the identical N9-attached moiety in PU-H54 and makes no stabilizing interactions with the protein (**Figure 3a**). However, because the N3-attached tail is more interior to the ATP binding pocket compared to the N9-attached tail of PU-H54, the displacement and disorganization of the nearby solvent molecules is less than that seen in Hsp90:PU-H54. This may explain the slightly better binding of PU-H36 to Hsp90 than PU-H54.

Unlike the Grp94-selective PU-H36, the pan-hsp90 inhibitor PU-H71 binds with nanomolar affinity to all hsp90 paralogs (**Figure 1**) (23,26). A notable difference between PU-H71 and the Grp94-selective PU compounds is the larger 8-aryl group, which contains both a 2' iodine along

with a 4'5'-methylenedioxy cap. While both PU-H71 and PU-H36 are Hsp90 Site 1 binders, PU-H71 binds to Hsp90 with 10^3-10^4 fold higher affinity than PU-H36 (**Figure 1**). Compared to PU-H36, PU-H71 forms a more extensive set of protein-ligand interactions within the Hsp90 ATP binding pocket than PU-H36 and provides a rationale for the observed difference in binding (**Figure 4a**). In particular, the bicyclic 8-aryl of PU-H71 allows it to make extensive pi-pi contacts with Phe138 and with both rings of Trp162. In addition, the 2'-iodine forms a water mediated hydrogen bond with the Leu107 backbone oxygen (26). These stabilizing interactions are not allowed by PU-H36 since its 8-aryl moiety is smaller and does not have any polar or charged functionality. The curled tail conformation of PU-H36 when bound to Hsp90 (**Figure 3a**) also differs from the extended trimethylamine tail of PU-H71. The charged tail of PU-H71 not only increases its solubility, but it also allows for additional hydrogen bond interactions in the pocket. The hydrophobic alkyl tail and 8-aryl moiety of PU-H36 cannot duplicate these stabilizing interactions shown by PU-H71.

Structure of Grp94N with PU-H71 reveals Site 1 binding.

Unlike PU-H36 and PU-H54, which bind to Grp94 better than Hsp90, PU-H71 exhibits a greater affinity for Hsp90 over Grp94. In Hsp90 the 8-aryl group is inserted into Site 1 and derives its high affinity from extensive contacts in that pocket. For Grp94, modeling studies show that the 8-aryl group of PU-H71 could be accommodated into Site 1 or Site 2 although the fit into the later may be sub-optimal due to a predicted close contact between the methylenedioxy group and Gly198. In order to understand how PU-H71 binds to Grp94, we determined the co-crystal structure of PU-H71 in complex with Grp94 at 1.72 Å resolution.

The structure of Grp94N:PU-H71 (**Figure 4b**) reveals that the 8-aryl group of PU-H71 is inserted into Site 1 of the Grp94 ATP binding pocket. Site 2 remains closed, and without the extensive rearrangements needed to accommodate the movement of Phe199, Tyr200, and H1, the overall protein conformation is similar to that of apo-Grp94 (PDB code 1yt1). A small unwinding at the end of H3 involving residues 161-163 occurs as a consequence of accommodating the larger 8-aryl moiety in Site 1. Density corresponding to residues 164-187 of H4 was observed during refinement but the quality was insufficient to include in the final model.

When bound to Grp94, PU-H71 adopts a pose similar to that found in Hsp90 (**Figure 4a, 4c**). An identical architecture of stabilizing interactions found in Hsp90:PU-H71 is also observed in Grp94:PU-H71, including hydrogen-bonding of the purine N6 with Asp149, water-mediated H-bonds to Leu104, Asn107, Val147, Asp149, Gly153, and Thr245, and the hydrophobic contacts between Met154 as well as Ala111 and the adenine ring. Similar to that found in Hsp90:PU-H71, the ligand displays an extensive network of pi-pi interactions with Phe199, Tyr200, and Tryp223. Thus the same factors that allow PU-H71 to achieve nanomolar binding to Hsp90 are also at work in binding to Grp94. However, the partial disorder of H4 of Grp94, as was noted previously for the compound SNX-0723 (27), likely exacts an energetic penalty by weakening the interactions in the adjacent Site 1, leading to the observed decrease in binding relative to Hsp90 (**Figure 1**).

Opening up Site 2 in Hsp90.

Strand 1 and Helix 1 (S1/H1) are part of the mobile lid substructure in Grp94, which exhibits a variety of conformations dictated by ligands, particularly Site 2 binders, as they bind in the ATP pocket. The Grp94 structures co-crystallized with Site 2 ligands (PU-H54, PU-H36, BnIm, Bis-methylester-BnIm, Bis-chloro-BnIm) (15,19) reveal that access to Site 2 depends on the backbone of Phe199 moving 2.8 Å away from its apo position and the side chain rotating ~25 degrees to allow for a hydrophobic moiety to be inserted into this exposed pocket. The movement of Phe199 forces Tyr200 to shift in order to prevent steric clashes, ultimately triggering a cascade of conformational rearrangements involving S1/H1 and the neighboring helices H4 and H5, resulting in Grp94 lid conformations that are significantly different from that found in the apo or ATP-bound protein. In Hsp90, a similar flexibility of S1/H1 has not been observed, and the Grp94 Site 2-targeted moieties of ligands, such as the 8-aryl groups of PU-H54 and PU-H36, are confined to Site 1 in this paralog.

Earlier attempts to rationalize the flexibility of the Grp94 lid, compared to Hsp90, proposed that the 5 amino acid insertion in H4 that is not found in Hsp90 destabilized the Grp94 lid and provided a lower energetic barrier to its rearrangement (22). However, because the repositioning of S1/H1 is the third downstream structural consequence following the movements of Phe199 and Tyr200, we asked whether differences in S1/H1 alone were sufficient to allow access to Site 2. The S1/H1 segment consists of 27 amino acids, of which 13 differ between Hsp90 and Grp94 (**Figure 5a**). To test this hypothesis, we created chimeric proteins, termed $Hsp90^{grpS1/H1}$ and $Grp94^{hspS1/H1}$, where S1/H1 from one paralog was substituted with S1/H1 from the other. We then used ITC to test the effect of the swap on the binding of inhibitors that preferred or required access to Site 2 for binding. We tested two different Site 2 inhibitors: 1) Bis-methylester BnIm (bme-BnIm), an inhibitor whose 1- and 3-methyl ester moieties on the resorcinylic scaffold require it to interact with Site 2 and exhibits no detectable binding to Hsp90 by ITC (**Figure 1**); and 2) PU-H36, which exhibits 10-fold selectivity for Grp94 when its 8-aryl group is inserted into Site 2, compared to its binding to Site 1 in Hsp90. As controls, we tested Radicicol, a high affinity inhibitor that binds in the ATP pocket but does not utilize either Site 1 or Site 2, and PU-H71, a high affinity non-selective inhibitor that binds in Site 1. With the structural data provided above, all four ligands have crystal structures in complex with Grp94 and with Hsp90 (Grp94:bme-BnIm PDB code 6baw; Hsp90:bme-BnIm PDB code 6ceo; Grp94:Radicicol PDB code 1u0z; Hsp90:Radicicol PDB code 4egk; Hsp90:PU-H71 PDB code 2fwz) (19,22,26,28), allowing us to correlate S1/H1 and ATP pocket remodeling with binding affinity.

The binding of the resorcinylic inhibitor bme-BnIm to Grp94 triggers Site 2 pocket availability and lid remodeling (19). The resorcinylic ring of bme-BnIm sits in the main cavity and the 1-methyl ester is inserted into Site 2. The benzyl imidazole is situated in Site 1 and the lid adopts a different conformation relative to the apo protein. Hsp90 cannot bind bme-BnIm in a manner that allows the resorcinylic group to achieve stable interactions with the ATP binding cavity. This

failure, as shown by the dramatic loss of enthalpy and affinity in ITC assays, stems from the inability of Hsp90 to relieve the steric clash between the side chain of Phe138 and the resorcinylic methyl esters. The crystal structure of bme-BnIm bound to Hsp90 confirmed that the resorcinylic scaffold is displaced in the binding pocket and the pendant benzyl imidazole is disordered, all of which are hallmarks of non-specific binding. Because there is no low-affinity alternate pose available, as in the case of the PU compounds, bme-BnIm can be used to probe the effect of a S1/H1 swap on the plasticity of the binding pocket, particularly Site 2, in the Hsp90$^{grpS1/H1}$ and Grp94$^{hspS1/H1}$ chimeras.

The ITC thermograms of WT Hsp90 compared to chimeric Hsp90$^{grpS1/H1}$ with bme-BnIm show a change from a flat binding curve with very small enthalpy to a sigmoidal one representing a binding event (**Figure 5c**). A large gain in binding affinity for the ligand by the chimeric Hsp90$^{grpS1/H1}$ is also noted when compared to WT Hsp90 (**Table 1**). Because the resorcinylic scaffold can only make productive interactions with the binding pocket when the 1-methyl-ester inserts into Site 2, this change in affinity suggests that Site 2 in chimeric Hsp90$^{grpS1/H1}$ has opened up as a consequence of the S1/H1 swap. Interestingly, the K_d of chimeric Hsp90$^{grpS1/H1}$ for bme-BnIm (1.3 μM) is slightly better than that of WT Grp94 (4.2 μM), possibly reflecting the improved stabilization of the benzyl imidazole in Site 1 of Hsp90 compared to WT Grp94, where part of H4 is disordered (19).

The opposite effect is observed when the Hsp90-derived S1/H1 is substituted into Grp94. Compared to the increase in affinity seen in Hsp90$^{grpS1/H1}$, a ~5-fold decrease in affinity for bme-BnIm is noted with Grp94$^{hspS1/H1}$. The apparent enthalpy is also much less than that with WT Grp94 (**Figure 5c, Table 1**). This suggests that, compared to WT Grp94, chimeric Grp94$^{hspS1/H1}$ has a modified binding pocket most likely involving a loss of access to Site 2 that reduces the affinity of the inhibitor. This outcome can be directly ascribed to the swapped S1/H1. The changes in the binding pocket may result in a non-optimal accommodation of the resorcinylic scaffold in the cavity, such as that shown in the Hsp90:bme-BnIm structure (19).

PU-H36 binds to Grp94 with a K_d of 2.6 μM and to Hsp90 ~10 fold less tightly (**Figure 5c, Table 1**). When S1/H1 is swapped, PU-H36 binding to the chimeric Hsp90 with S1/H1 from Grp94 (Hsp90$^{grpS1/H1}$) improves from a K_d of 28 μM in WT to a K_d of 7.6 μM. The observed gain in affinity for PU-H36 by Hsp90$^{grpS1/H1}$ suggests that chimeric Hsp90$^{grpS1/H1}$ has acquired a different mode of binding for PU-H36. This is consistent with the conformational flexibility of S1/H1 from Grp94 being imparted to Hsp90$^{grpS1/H1}$, thereby allowing the 8-aryl group of PU-H36 to access Site 2 of the chimera.

In contrast, the corresponding Grp94 chimera, Grp94 with S1/H1 from Hsp90 (Grp94$^{hspS1/H1}$) exhibits a K_d of 6.1 μM for PU-H36, which is a 2.4-fold loss in affinity relative to WT Grp94. This suggests that PU-H36 is not in the same pose observed in WT Grp94 and that an alteration in how the 8-aryl moiety is accommodated in the cavity of Grp94$^{hspS1/H1}$ has occurred. If the 8-aryl moiety of PU-H36 has transitioned into Site 1 of chimeric Grp94$^{hspS1/H1}$, this change from the

hydrophobic Site 2 pocket to a more solvent accessible environment in Site 1 would extract an energetic penalty that could explain the loss of affinity compared to WT.

In control experiments, both Grp94$^{hspS1/H1}$and Hsp90$^{grpS1/H1}$ displayed a small loss in binding for radicicol but retained tight nanomolar affinity (**Table 1**). This indicates a minor role for S1/H1 in situating radicicol within the ATP binding pocket, which agrees with the structures of the Grp94:radicicol and Hsp90:radiciciol complexes. In addition, these results show that the main cavity is undisturbed by the S1/H1 swap. Similarly, the two chimeras exhibit only minor gains in their binding to PU-H71. The measured K_d of PU-H71 to WT Hsp90 is 5.3 nM while its K_d to chimeric Hsp90$^{grpS1/H1}$ is 3.7 nM. Meanwhile chimeric Grp94$^{hspS1/H1}$ showed a similar small change in K_d (27.2 nM) relative to that of WT Grp94 (48.7 nM). The small change in K_d between these chimeras and the WT proteins is not surprising because, as a Site 1 binder, PU-H71 does not precipitate structural changes involving S1/H1 in either Hsp90 or Grp94. In particular, PU-H71 binding does not perturb the position of the Phe138 side chain relative to the unbound protein. The crystal structure of Grp94 with PU-H71 described above helps to clarify the ITC data obtained with chimeric Grp94$^{hspS1/H1}$ by showing that PU-H71 binding does not change the conformation of H1 relative to that in apo Grp94 (**Figure 4b**). Thus, both the ITC and structural data reveal that S1/H1 does not play a major role in stabilizing and binding of Site 1 inhibitors.

Discussion

In this report we have shown that an NTD segment comprised of H1 and S1 are the determinants of whether the NTD ATP binding pocket can undergo the conformational shifts needed to expose Site 2 upon ligand binding. These studies take advantage of the availability of a chemical tool set comprised of Grp94-selective and non-selective inhibitors, and its usefulness is enhanced when coupled with crystal structures in complex with Hsp90 and Grp94 that reveal their modes of binding.

The results presented here contrast with earlier speculation that the difference allowing the exposure of Site 2 in Grp94 resided in the five amino acid insertion that extends H4 in Grp94, an insertion that is not found in Hsp90 (15,17,22). To access Site 2, Phe199 is repositioned to uncover the mouth of the Site. This movement is predicated on the ability of the adjacent residue, Tyr200, to move in concert with Phe199. In the apo Grp94 NTD, Tyr200 is constrained by the position of H1, so the exposure of Site 2 ultimately depends on relieving the constraints imposed on Tyr200 by H1. The equivalent residues in Hsp90, Phe138 and Tyr139, occupy nearly identical positions to Phe199 and Tyr200 in apo Grp94. Because Site 2 remains closed in Hsp90, this suggests that the constraints imposed on Tyr139 by H1 cannot be relieved. In Grp94, all of the structures of ligand complexes where Site 2 is exposed (Grp94:PU-H54, Grp94:BnIm, Grp94:bme-BnIm, Grp94:PU-H36) (15,19) display very large repositioning movements of H1, supporting the notion that the movement of this structural element is important for Site 2 opening.

We can get insight into the origins of the different role S1/H1 plays in the two paralogs by comparing the structures of the unliganded NTDs from Grp94 (PDB code 1yt2) and Hsp90 (PDB code 1yer, 1yes). These structures show that S1 (Grp94 residues 69-78, Hsp90 residues 13-22) is unlikely to play a role in regulating access to Site 2. The structures of S1 from the two paralogs are superimposable, and the five residues that differ between Grp94 and Hsp90 in this region are solvent exposed and make no discriminating interactions. On the other hand, the position of H1 in the two paralogs differs, suggesting that this region is likely to be the discriminating element. The Grp94 and Hsp90 H1s overlap at their N-termini (Grp94 Ala80/Hsp90 Ala24), but the Grp94 H1 is longer than the Hsp90 H1 by a half turn, and the trajectories of their axes diverge by ~16 degrees, such that by their C-termini (Grp94 Leu93/Hsp90 Phe37), the two Cα positions are separated by 7.3 Å (**Figure 6a**). This places H1 of Grp94 closer to H4 of the NTD than H1 of Hsp90 is to the equivalent H4 in Hsp90.

If we posit, based on the S1/H1 swap results presented here, that the Hsp90 conformation of H1 is more stable than the Grp94 conformation and less susceptible to movement, we can ask what sequence differences permit one paralog to adopt the more stable conformation while the other adopts the less stable position? H1 is comprised of 14 amino acids, of which seven differ between Hsp90 and Grp94 (**Figure 5a**). Four of these differences are likely to be inconsequential due to surface exposure or lack of significant interactions. Three pairs of differing residues, however - Grp94 Met85/Hsp90 Leu29 (P1), Ser92/Thr36 (P2), and Leu93/Phe37 (P3) – make interactions with or are closely packed at the interface with the body of the NTD (**Figure 6**). To understand whether these three differing pairs of residues can account for the different behaviors of H1, we modeled Grp94 H1 into Hsp90, and Hsp90 H1 into Grp94. We tested the modeling in both positions of H1 – the stable Hsp90 position, and the lower stability Grp94 position. From this analysis, numerous steric incompatibilities are apparent (**Figure 6d**). First, if the Hsp90 H1 replaces Grp94 H1 when H1 is in the (unstable) Grp94 position, P1, P2, and P3 (Met85Leu, Ser92Thr, Leu93Phe) exhibit clashes with Grp94 residues Ile90, Tyr200, Thr188, Ser189, and Ile192. These clashes can be completely relieved if the Hsp90 H1 is transferred to the (stable) Hsp90 position, showing that Hsp90 H1 is compatible with the body of the Grp94 NTD, but only in the Hsp90 H1 position. Thus, the modeling predicts that Hsp90 H1 can only adopt the stable configuration but not the unstable position when incorporated into Grp94. This supports the experimental data presented above, where the chimeric Grp94$^{hspS1/H1}$ behaved as if Site 2 was no longer accessible to Site 2 binding ligands.

Conversely, if Grp94 H1 is incorporated into Hsp90, H1 is incompatible with the stable position because P3 (Leu29Met) would clash with residues Thr115, Phe118, and Met119 of Hsp90 H5. The relief of these clashes would require H1 to move away from the body of the NTD, pushing it away from the stable position. This is in agreement with the experimental data showing that chimeric Hsp90$^{grpS1/H1}$ is accessible to Site 2 binding ligands. Interestingly, if the Grp94 H1 is placed in the unstable Grp94 position, clashes are also observed between P1, P2, and P3 and Ala111, Thr115, Val136, Ile128, Leu122, Ile43, and Ile128 of the Hsp90 NTD. This suggests that a different unstable position for Grp94 H1 is achieved in the Hsp90$^{grpS1/H1}$ chimera.

Together, these modeling studies explain how the sequence of Grp94 H1 dictates its placement into a position of lower stability, thus precipitating its movement to expose Site 2 upon selective ligand binding.

The effect of a H1 swap between Grp94 and Hsp90 on the binding of Site 2 selective ligands, and the modeling above suggests that H1 plays a significant role in permitting the remodeling of the ATP binding pocket that drives paralog selective ligand affinity. Site 2 binding is not observed in human Hsp90, but the structure of Hsp90 from the fungus *Candida albicans* bound to the fungal-selective ligand CMLD013075 (PDB code 6cjp) (25) revealed that CMLD013075 binds to Site 2 and that the position of H1 resembles that seen in Grp94:PU-H36. To accommodate the 4-methoxybenzyl moiety in Site 2, *Candida* Hsp90 Phe127 and Tyr128 (equivalent to Grp94 Phe199 and Tyr200) move away from their pocket-occluding apo positions (PDB code 6cji), thereby precipitating the change in H1 conformation. A comparison of the three H1 residue positions that were identified in the modeling above as determinants of H1 movement shows that while P1 and P2 in *Candida* Hsp90 are identical to their human Hsp90 counterparts, the P3 pair (*Hs*Hsp90 Phe37/*Ca*Hsp90 Val26), differs (**Figure 5b**). In the apo configuration, H1 from human and *Candida* Hsp90 overlap. However, in the CMLD013075-bound structure, H1 is extended at its C-terminus such that Val26 faces H5. Modeling a phenylalanine in place of valine in this conformation predicts a clash with Leu111 of H5. Thus, it appears that P3, the sensitive H1 position in *Candida* Hsp90, allows for movement of H1 by favorably repositioning Val26.

The role of H1 in directing Site 2 access in *Candida* Hsp90 is further supported by the reported mutagenesis data, where a Phe131Tyr mutation in the body of the NTD reduces the sensitivity to CMDL013075 (25). From the structure, the Phe131Tyr mutation appears to stabilize the interaction with Met19 of H1, thereby providing a greater energetic barrier to H1 movement and Site 2 exposure. Finally, it was also noted that CMDL013075 was effective growth suppressor of yeast Hsc82. Yeast Hsc82 also has a valine at P3, the third sensitive H1 position (**Figure 5b**), supporting the notion that this lowers the barrier to H1 rearrangement in a manner similar to that of *Candida* Hsp90 upon Site 2 binding ligands. Interestingly, a comparison of Hsp90 from multiple organisms (29) shows that the incorporation of phenylalanine at P3 is a relatively recent adaptation that is specific to metazoans and higher eukaryotes, suggesting that there is an evolutionary benefit to stiffening the interaction between H1 and the body of the NTD.

In a similar manner, an examination of H1 from Trap1 and *E.coli* HtpG, paralogs that, along with Grp94 are evolutionarily older than eukaryotic Hsp90, indicates that two of the 3 discriminating residues differ from the stable set seen for Hsp90 (**Figure 5b**). In both Trap1 and HtpG, P2 and P3 are Ser-Leu, which is identical to P2 and P3 seen in Grp94. The prediction is that H1 in these proteins would also allow the ATP pocket remodeling to expose Site 2. In support of this, FP competition assays of Grp94-selective PU compounds consistently showed binding to Trap1 that was significantly stronger than to Hsp90, suggesting that these compounds accessed Site 2 in Trap1 (15,17), albeit with a higher energetic penalty than in Grp94.

Recently a novel ATP pocket rearrangement was observed in the structure of human Hsp90 in complex with KUNA-111, an Hsp90-selective, tertiary alcohol inhibitor (PDB code 7ur3) (30). In this structure, the side chain of Phe138 adopts a new rotomeric position such that the edge-on-pi interaction with Tyr139 was replaced by a pi-pi interaction with the same residue, thus expanding the volume of Site 1 to accommodate the bulky phenylpropyl substituent. Notably, however, the position of Tyr139 was not perturbed by this new rotomeric position of Phe138, nor was the position or conformation of H1. Modeling of PU-H36 and bme-BnIm into the Hsp90:KUNA-111 structure shows that despite its large rotation, the movement of Phe138 is insufficient to expose Site 2, with steric clashes predicted between the 8-aryl and methylester substituents of these ligands, and the Phe138 beta carbon. Thus, although a novel repositioning of Phe138 has for the first time been observed in human Hsp90, the exposure of Site 2 still appears to require the coordinated movement of the adjacent Tyr139 and H1.

Overall, our results highlight the influence of H1 in allowing access to the Site 2 pocket. Chaperones with conformationally flexible H1s are sensitive to ligands that target this pocket while those with a more rigid H1 attachment to the body of the NTD are not sensitive. The H1 acts as a selectivity module, and when the relatively immobile H1 of Hsp90 is replaced by the more conformationally flexible equivalent H1 of Grp94, Hsp90 adopts a Grp94-like mode of binding that includes exposing the hydrophobic Site 2 pocket. Identifying the structural drivers of ligand sensitivity, however, is just one component of solving the puzzle of therapeutic targeting of Grp94. A view is now emerging that multiple structural forms of Grp94 exist in disease, and that these forms are driven in part by post-translational modifications such as *N*-glycosylation and subsequent organization of the chaperone into multi-component epichaperome structures (31,32). Further studies will be required to understand how these epigenetic regulatory mechanisms influence the structure of Grp94 and restrict or enhance the access of ligands to selective, targetable side pockets.

Experimental Procedures

Protein purification. Canine Grp94, which is 98% identical with human Grp94, residues 69–337 with the charged linker (residues 287–327) replaced with 4 Glycines (Grp94NΔ41) was overexpressed in *E. coli* strains BL21 Star (DE3) and purified as previously described (22). The purified protein was stored in 10 mM Tris, pH 7.6, 100 mM NaCl, 1 mM DTT at 30 mg/ml were stored at -80 °C. The N-terminal domain of human Hsp90α residues 1–236 (Hsp90N) was over-expressed and purified as previously described (19). The purified protein was concentrated to 20-30 mg/mL and stored at -80 °C in a buffer of 10 mm Tris, pH 7.6, 100 mM NaCl, and 1 mM DTT.

Ligands. PU-H36, PU-H54, and PU-H71 were synthesized as previously reported (15,33) and were dissolved in DMSO, typically at concentrations of 50-100 mM. bme-BnIm was a gift from Dr. Brian Blagg (University of Notre Dame). Radicicol was purchased from Sigma.

Crystallization. Protein:ligand complexes were formed by mixing a three to five-fold molar excess of inhibitor to the concentrated protein and incubating the mixture for one hour. Initial crystallization conditions were identified using a high throughput screen at the HWI National Crystallization Center (34). Crystallizations were carried out using the hanging drop vapor diffusion method using equal volumes of reservoir cocktail and inhibitor-protein solution.

Crystals of Hsp90N:PU-H36 grew at 4 ^{o}C over a reservoir containing 0.1 M sodium cacodylate (pH 6.5), 0.18-0.22 M $MgCl_2$, and 8-25% polyethylene glycol 2000 monomethyl ether (PEG 2K MME). Crystals typically appeared in 1-2 days and were cryoprotected by rapid sequential passage through the reservoir solution followed by the reservoir cocktail where the PEG 2K MME was increased to 35%. Cryoprotected crystals were recovered in nylon loops and immediately flash cooled in liquid nitrogen.

S1/H1 chimeras. All chimeras were generated by cross-over PCR reactions. The Grp94N$^{hspS1/H1}$ chimera is Grp94N (69-337Δ41) with residues 69-95 replaced with Hsp90 residues 1-39. Hsp90$^{grpS1/H1}$ chimera is Hsp90 (1-236) with residues 1-39 replaced by Grp94 residues 69-95. Chimeric protein expression and purification was as described above.

Isothermal Titration Calorimetry. ITC titrations were carried out on a VP-ITC (Microcal) at 25 ^{o}C as previously described (19). The feedback mode was set to high and the reference power set at 10 μCal. For most of the titrations, the protein solution was loaded in the syringe and the inhibitor in the cell. Both protein and inhibitor solutions were prepared in matched buffers of 40 mM Hepes (pH 7.5), 100 mM NaCl, and 2% DMSO. Titrations involved 29 injections of 10 μL (2 μL for the first injection) set 5 minutes apart and stirring speed set at 310 rpm. The first injection was discarded in all titrations. If saturation was achieved, heats of dilution were estimated from the final injections, otherwise a protein into buffer background titration was performed. Data were fit to a one-site model using Origin. Titrations at higher DMSO (4-5%) or in other buffers were also carried out using the same parameters described above.

Data collection and structure refinement. X-ray diffraction data was collected at SSRL beamline 9-2 and APS beamline 23-ID-B. Data were reduced and scaled using either HKL2000 or AutoProc 1.0.5 (35-37). Structures were solved by molecular replacement with either PDB 2FWZ as the search model for Hsp90N or the core region of Grp94 for Grp94N crystals. Missing residues were manually rebuilt and refined by using COOT and PHENIX (38,39). Inhibitor and solvent positions were identified from overlapping peaks of difference density**.** Ligand parameter and topology files were generated using Phenix eLBOW or the Dundee PRODRG server (40). Structure validation was performed with MolProbity (41). Data collection and refinement statistics are shown in **Table 2**. Molecular graphics were generated using PyMOL (Schrodinger, Inc).

Data Availability

Crystal structure data and coordinates have been deposited with the Protein Data Bank under accession codes 8SBT, 8TF0, and 8SSV.

Acknowledgements

We thank Kevin Maharaj for help with the PU-H36 structure refinement and the National Crystallization Center personnel for their help with crystallization screening. X-ray diffraction data was collected at the Advanced Photon Source beamline 23-IDB, and the Stanford Synchrotron Radiation Lab beamline BL9-2. Screening for crystal diffraction was performed at CHESS beamline ID7B2.

Author contributions

N.L.S.Q. designed and performed all experiments with input from D.T.G. G.C. provided the PU compounds. P.M.S. carried out the PU-H54 ITC titrations. W.A. helped prepare proteins. N.L.S.Q. and D.T.G. analyzed data. N.L.S.Q. wrote the original the draft of the manuscript. N.L.S.Q. and D.T.G. revised the manuscript.

Funding

Supported by grants R01-CA095130 and P01-CA186866 from the NIH. Crystallization screening was carried out at the National Crystallization Center at HWI which is supported by NIH grant R24GM141256. The content is solely the responsibility of the authors and does not necessarily represent the official views of the National Institutes of Health.

Conflict of Interest

G. Chiosis is an inventor on patents covering purine-scaffold Hsp90 inhibitors. G. Chiosis is a founder of Samus Therapeutics.

References

1. Echeverria, P. C., Bernthaler, A., Dupuis, P., Mayer, B., and Picard, D. (2011) An interaction network predicted from public data as a discovery tool: application to the Hsp90 molecular chaperone machine. *PLoS One* **6**, e26044

2. Taipale, M., Jarosz, D. F., and Lindquist, S. (2010) HSP90 at the hub of protein homeostasis: emerging mechanistic insights. *Nat Rev Mol Cell Biol* **11**, 515-528

3. Schopf, F. H., Biebl, M. M., and Buchner, J. (2017) The HSP90 chaperone machinery. *Nature Reviews Molecular Cell Biology* **18**, 345

4. Ansa-Addo, E. A., Thaxton, J., Hong, F., Wu, B. X., Zhang, Y., Fugle, C. W., Metelli, A., Riesenberg, B., Williams, K., Gewirth, D. T., Chiosis, G., Liu, B., and Li, Z. (2016) Clients and Oncogenic Roles of Molecular Chaperone gp96/grp94. *Current topics in medicinal chemistry* **16**, 2765-2778

5. Gewirth, D. T. (2016) Paralog Specific Hsp90 Inhibitors - A Brief History and a Bright Future. *Current topics in medicinal chemistry* **16**, 2779-2791

6. Valastyan, J. S., and Lindquist, S. (2014) Mechanisms of protein-folding diseases at a glance. *Dis Model Mech* **7**, 9-14

7. Sanchez, J., Carter, T. R., Cohen, M. S., and Blagg, B. S. J. (2020) Old and New Approaches to Target the Hsp90 Chaperone. *Curr Cancer Drug Targets* **20**, 253-270

8. Dekker, F. A., and Rudiger, S. G. D. (2021) The Mitochondrial Hsp90 TRAP1 and Alzheimer's Disease. *Front Mol Biosci* **8**, 697913

9. Xie, S., Wang, X., Gan, S., Tang, X., Kang, X., and Zhu, S. (2020) The Mitochondrial Chaperone TRAP1 as a Candidate Target of Oncotherapy. *Front Oncol* **10**, 585047

10. Southworth, D. R., and Agard, D. A. (2011) Client-loading conformation of the Hsp90 molecular chaperone revealed in the cryo-EM structure of the human Hsp90:Hop complex. *Molecular cell* **42**, 771-781

11. Dollins, D. E., Warren, J. J., Immormino, R. M., and Gewirth, D. T. (2007) Structures of GRP94-nucleotide complexes reveal mechanistic differences between the hsp90 chaperones. *Molecular cell* **28**, 41-56

12. Huck, J. D., Que, N. L., Hong, F., Li, Z., and Gewirth, D. T. (2017) Structural and Functional Analysis of GRP94 in the Closed State Reveals an Essential Role for the Pre-N Domain and a Potential Client-Binding Site. *Cell Rep* **20**, 2800-2809

13. Jhaveri, K., Taldone, T., Modi, S., and Chiosis, G. (2012) Advances in the clinical development of heat shock protein 90 (Hsp90) inhibitors in cancers. *Biochimica et biophysica acta* **1823**, 742-755

14. Yuno, A., Lee, M. J., Lee, S., Tomita, Y., Rekhtman, D., Moore, B., and Trepel, J. B. (2018) Clinical Evaluation and Biomarker Profiling of Hsp90 Inhibitors. *Methods Mol Biol* **1709**, 423-441

15. Patel, P. D., Yan, P., Seidler, P. M., Patel, H. J., Sun, W., Yang, C., Que, N. S., Taldone, T., Finotti, P., Stephani, R. A., Gewirth, D. T., and Chiosis, G. (2013) Paralog-selective Hsp90 inhibitors define tumor-specific regulation of HER2. *Nat Chem Biol* **9**, 677-684

16. Taldone, T., Patel, P. D., Patel, M., Patel, H. J., Evans, C. E., Rodina, A., Ochiana, S., Shah, S. K., Uddin, M., Gewirth, D., and Chiosis, G. (2013) Experimental and structural testing module to analyze paralogue-specificity and affinity in the Hsp90 inhibitors series. *J Med Chem* **56**, 6803-6818

17. Patel, H. J., Patel, P. D., Ochiana, S. O., Yan, P., Sun, W., Patel, M. R., Shah, S. K., Tramentozzi, E., Brooks, J., Bolaender, A., Shrestha, L., Stephani, R., Finotti, P., Leifer, C., Li, Z., Gewirth, D. T., Taldone, T., and Chiosis, G. (2015) Structure-activity relationship in a purine-scaffold compound series with selectivity for the endoplasmic reticulum Hsp90 paralog Grp94. *J Med Chem* **58**, 3922-3943

18. Jiang, F., Guo, A. P., Xu, J. C., You, Q. D., and Xu, X. L. (2018) Discovery of a Potent Grp94 Selective Inhibitor with Anti-Inflammatory Efficacy in a Mouse Model of Ulcerative Colitis. *J Med Chem* **61**, 9513-9533

19. Que, N. L. S., Crowley, V. M., Duerfeldt, A. S., Zhao, J., Kent, C. N., Blagg, B. S. J., and Gewirth, D. T. (2018) Structure Based Design of a Grp94-Selective Inhibitor: Exploiting a Key Residue in Grp94 To Optimize Paralog-Selective Binding. *J Med Chem* **61**, 2793-2805

20. Mishra, S. J., Khandelwal, A., Banerjee, M., Balch, M., Peng, S., Davis, R. E., Merfeld, T., Munthali, V., Deng, J., Matts, R. L., and Blagg, B. S. J. (2021) Selective Inhibition of the Hsp90alpha Isoform. *Angew Chem Int Ed Engl* **60**, 10547-10551

21. Mishra, S. J., Liu, W., Beebe, K., Banerjee, M., Kent, C. N., Munthali, V., Koren, J., 3rd, Taylor, J. A., 3rd, Neckers, L. M., Holzbeierlein, J., and Blagg, B. S. J. (2021) The Development of Hsp90beta-Selective Inhibitors to Overcome Detriments Associated with pan-Hsp90 Inhibition. *J Med Chem* **64**, 1545-1557

22. Soldano, K. L., Jivan, A., Nicchitta, C. V., and Gewirth, D. T. (2003) Structure of the N-terminal domain of GRP94. Basis for ligand specificity and regulation. *The Journal of biological chemistry* **278**, 48330-48338

23. Huck, J. D., Que, N. L. S., Immormino, R. M., Shrestha, L., Taldone, T., Chiosis, G., and Gewirth, D. T. (2019) NECA derivatives exploit the paralog-specific properties of the site

3 side pocket of Grp94, the endoplasmic reticulum Hsp90. *The Journal of biological chemistry* **294**, 16010-16019

24. Immormino, R. M., Metzger, L. E. t., Reardon, P. N., Dollins, D. E., Blagg, B. S., and Gewirth, D. T. (2009) Different poses for ligand and chaperone in inhibitor-bound Hsp90 and GRP94: implications for paralog-specific drug design. *Journal of molecular biology* **388**, 1033-1042

25. Whitesell, L., Robbins, N., Huang, D. S., McLellan, C. A., Shekhar-Guturja, T., LeBlanc, E. V., Nation, C. S., Hui, R., Hutchinson, A., Collins, C., Chatterjee, S., Trilles, R., Xie, J. L., Krysan, D. J., Lindquist, S., Porco, J. A., Jr., Tatu, U., Brown, L. E., Pizarro, J., and Cowen, L. E. (2019) Structural basis for species-selective targeting of Hsp90 in a pathogenic fungus. *Nat Commun* **10**, 402

26. Immormino, R. M., Kang, Y., Chiosis, G., and Gewirth, D. T. (2006) Structural and quantum chemical studies of 8-aryl-sulfanyl adenine class Hsp90 inhibitors. *J Med Chem* **49**, 4953-4960

27. Ernst, J. T., Liu, M., Zuccola, H., Neubert, T., Beaumont, K., Turnbull, A., Kallel, A., Vought, B., and Stamos, D. (2014) Correlation between chemotype-dependent binding conformations of HSP90alpha/beta and isoform selectivity-implications for the structure-based design of HSP90alpha/beta selective inhibitors for treating neurodegenerative diseases. *Bioorg. Med. Chem. Lett.* **24**, 204-208

28. Austin, C., Pettit, S. N., Magnolo, S. K., Sanvoisin, J., Chen, W., Wood, S. P., Freeman, L. D., Pengelly, R. J., and Hughes, D. E. (2012) Fragment screening using capillary electrophoresis (CEfrag) for hit identification of heat shock protein 90 ATPase inhibitors. *J Biomol Screen* **17**, 868-876

29. Starr, T. N., Flynn, J. M., Mishra, P., Bolon, D. N. A., and Thornton, J. W. (2018) Pervasive contingency and entrenchment in a billion years of Hsp90 evolution. *Proceedings of the National Academy of Sciences of the United States of America* **115**, 4453-4458

30. Mishra, S. J., Reynolds, T. S., Merfeld, T., Balch, M., Peng, S., Deng, J., Matts, R., and Blagg, B. S. J. (2022) Structure-Activity Relationship Study of Tertiary Alcohol Hsp90alpha-Selective Inhibitors with Novel Binding Mode. *ACS Med Chem Lett* **13**, 1870-1878

31. Rodina, A., Wang, T., Yan, P., Gomes, E. D., Dunphy, M. P., Pillarsetty, N., Koren, J., Gerecitano, J. F., Taldone, T., Zong, H., Caldas-Lopes, E., Alpaugh, M., Corben, A., Riolo, M., Beattie, B., Pressl, C., Peter, R. I., Xu, C., Trondl, R., Patel, H. J., Shimizu, F., Bolaender, A., Yang, C., Panchal, P., Farooq, M. F., Kishinevsky, S., Modi, S., Lin, O., Chu, F., Patil, S., Erdjument-Bromage, H., Zanzonico, P., Hudis, C., Studer, L., Roboz, G. J., Cesarman, E., Cerchietti, L., Levine, R., Melnick, A., Larson, S. M., Lewis, J. S., Guzman, M. L., and Chiosis, G. (2016) The epichaperome is an integrated chaperome network that facilitates tumour survival. *Nature* **538**, 397-401

32. Yan, P., Patel, H. J., Sharma, S., Corben, A., Wang, T., Panchal, P., Yang, C., Sun, W., Araujo, T. L., Rodina, A., Joshi, S., Robzyk, K., Gandu, S., White, J. R., de Stanchina, E., Modi, S., Janjigian, Y. Y., Hill, E. G., Liu, B., Erdjument-Bromage, H., Neubert, T. A.,

Que, N. L. S., Li, Z., Gewirth, D. T., Taldone, T., and Chiosis, G. (2020) Molecular Stressors Engender Protein Connectivity Dysfunction through Aberrant N-Glycosylation of a Chaperone. *Cell Rep* **31**, 107840

33. He, H., Zatorska, D., Kim, J., Aguirre, J., Llauger, L., She, Y., Wu, N., Immormino, R. M., Gewirth, D. T., and Chiosis, G. (2006) Identification of potent water soluble purine-scaffold inhibitors of the heat shock protein 90. *J Med Chem* **49**, 381-390

34. Luft, J. R., Collins, R. J., Fehrman, N. A., Lauricella, A. M., Veatch, C. K., and DeTitta, G. T. (2003) A deliberate approach to screening for initial crystallization conditions of biological macromolecules. *J Struct Biol* **142**, 170-179

35. Otwinowski, Z., and Minor, W. (1997) Processing of X-ray diffraction data collected in oscillation mode. *Methods in Enzymology* **276**, 307-326

36. Vonrhein, C., Flensburg, C., Keller, P., Sharff, A., Smart, O., Paciorek, W., Womack, T., and Bricogne, G. (2011) Data processing and analysis with the autoPROC toolbox. *Acta crystallographica* **67**, 293-302

37. Tickle, I. J., Flensburg, C., Keller, P., Paciorek, W., Sharff, A., Vonrhein, C., and Bricogne, G. (2018) STARANISO. Global Phasing Ltd., Cambridge, United Kingdom

38. Liebschner, D., Afonine, P. V., Baker, M. L., Bunkoczi, G., Chen, V. B., Croll, T. I., Hintze, B., Hung, L. W., Jain, S., McCoy, A. J., Moriarty, N. W., Oeffner, R. D., Poon, B. K., Prisant, M. G., Read, R. J., Richardson, J. S., Richardson, D. C., Sammito, M. D., Sobolev, O. V., Stockwell, D. H., Terwilliger, T. C., Urzhumtsev, A. G., Videau, L. L., Williams, C. J., and Adams, P. D. (2019) Macromolecular structure determination using X-rays, neutrons and electrons: recent developments in Phenix. *Acta Crystallogr D Struct Biol* **75**, 861-877

39. Emsley, P., and Cowtan, K. (2004) Coot: model-building tools for molecular graphics. *Acta crystallographica* **60**, 2126-2132

40. Schuttelkopf, A. W., and van Aalten, D. M. (2004) PRODRG: a tool for high-throughput crystallography of protein-ligand complexes. *Acta Crystallogr. Sect. D Biol. Crystallogr.* **60**, 1355-1363

41. Chen, V. B., Arendall, W. B., 3rd, Headd, J. J., Keedy, D. A., Immormino, R. M., Kapral, G. J., Murray, L. W., Richardson, J. S., and Richardson, D. C. (2010) MolProbity: all-atom structure validation for macromolecular crystallography. *Acta Crystallogr. Sect. D Biol. Crystallogr.* **66**, 12-21

Figures

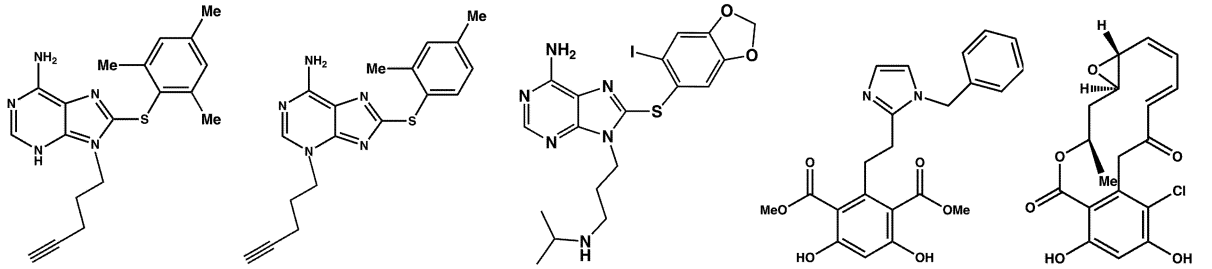

PU-H36
Hsp90 28
Grp94 2.6
Hsp/Grp 11

PU-H54
Hsp90 230
Grp94 69
Hsp/Grp 3.3

PU-H71
Hsp90 0.005
Grp94 0.049
Hsp/Grp 0.1

bme-Bnlm
Hsp90 n/d
Grp94 4.2
Hsp/Grp n/d

Radicicol
Hsp90 0.0004
Grp94 0.0015
Hsp/Grp 0.26

Figure 1. Ligands discussed in this report. Kd's for Hsp90 and Grp94 (μM) are from Table 1 and are listed below each compound.

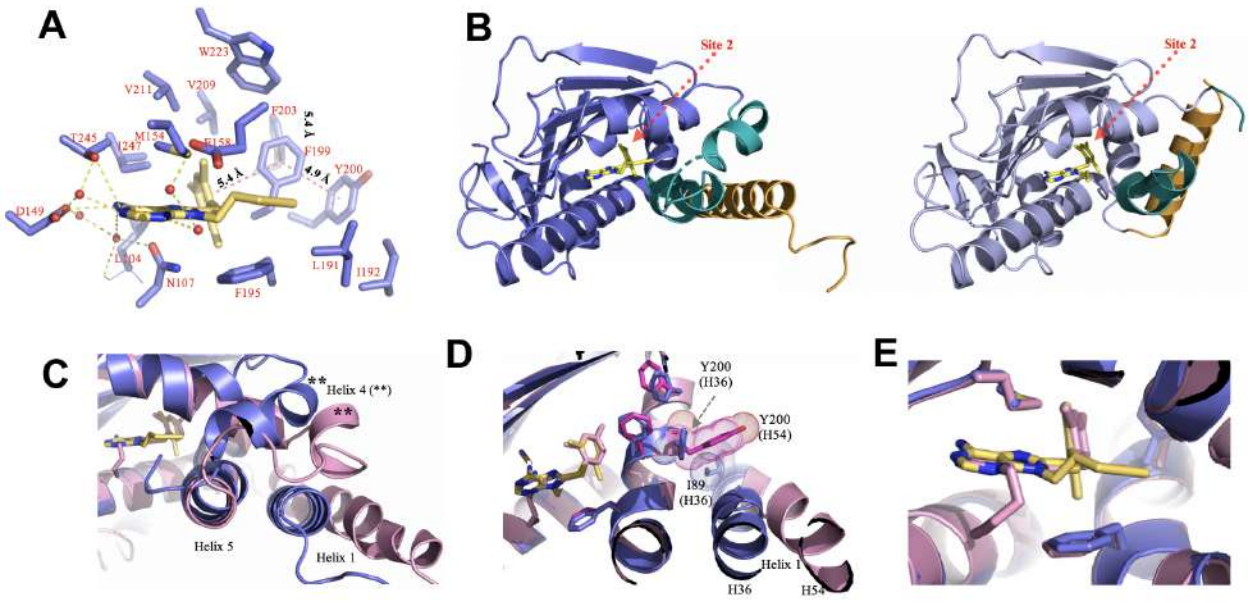

Figure 2. PU-H36 binds to Site 2 in Grp94. **(a)** PU-H36 in the binding cavity of Grp94N. The 8-aryl moiety is in the Site 2 pocket. A network of edge-on (perpendicular) Pi-Pi interactions centered on Phe199 is observed with the 8-aryl ring, Phe203, and Tyr200. **(b)** The two unique monomers in the GrpN94:PU-H36 crystallographic asymmetric unit show the lid conformations adopted by the protein with PU-H36 in the ATP binding pocket. H3 is yellow while H4 is shown in teal. **(c)** Overlay of Grp94N:PU-H36 (blue) with Grp94N:PU-H54 (pink) showing the different positions of H1. **(d)** The side chain of Tyr200 in Grp94:PU-H54 is rotated away from Phe199. This rotation forces H1 to shift further away from helix 6 in order to avoid a steric clash between the side chains of Tyr200 and Ile89. In Grp94:PU-H36, Tyr200 forms a pi-pi interaction with Phe199 and H1 remains attached to the body of the NTD. **(e)** The N9-acetylinic tail of PU-H36 makes van der Waals interactions with Phe195 and is inserted into a channel lined by Phe195, Phe199, Leu163, and Ile166. This channel is blocked in Grp94:PU-H54 (pink) by the side chain of Ile166. In contrast, the N-3 linked PU-H54 alkyl tail is tucked under the adenine and is projected towards helix 2. Note that Phe195 is superimposable in both structures.

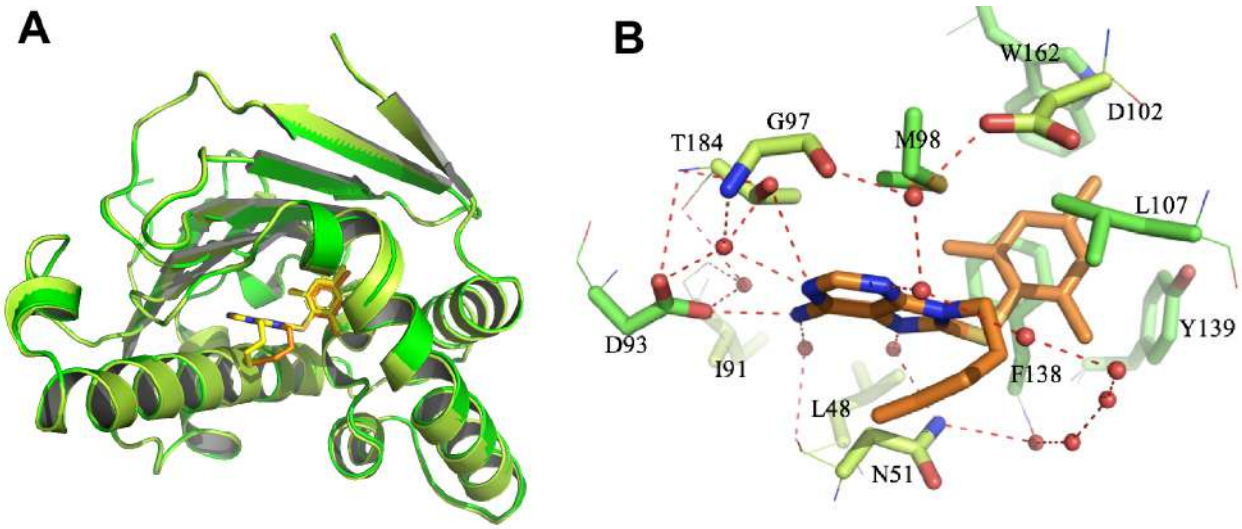

Figure 3. PU-H36 binds to Site 1 in Hsp90. **(a)** Superposition of Hsp90:PU-H36 (dark green, orange ligand) with Hsp90:PU-H54 (light green, yellow ligand). In both cases the 8-aryl moiety is in Site 1 and the alkyl tails adopt similar trajectories. **(b)** PU-H36 interactions in the ATP binding pocket. The 8-aryl moiety in Site 1 makes pi-pi interactions with Phe138 and Tyr139 and van der Waals contact with Leu107. The 5'-methyl sits above the adenine ring and forms a van der Waals contact. Leu107 makes a hydrophobic interaction with the 8-aryl ring.

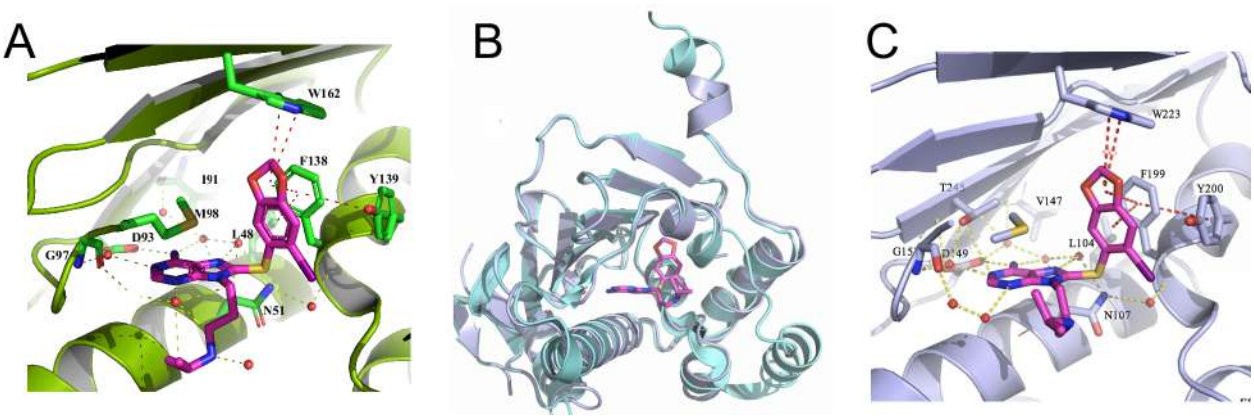

Figure 4. Grp94 binds PU-H71 in Site 1. **(a)** Interactions of PU-H71 with the Hsp90 ATP binding pocket. **(b)** The structure of Grp94N:PU-H71 (dark blue) is similar to apo GrpN94 (cyan). While H3/S1 of the lid was observed and can be superposed to that of the unliganded structure, portions of H4 and H5 in Grp94N:PU-H71 are disordered and are shown as dash lines; (**c)** PU-H71 in the Grp94 main pocket is stabilized by a network of hydrogen-bonds (yellow dashes), van der Waals and pi-pi interactions (red dashes). Phe199 is in the same position as in apo Grp94 and the 8-aryl of PU-H71 is found in Site 1.

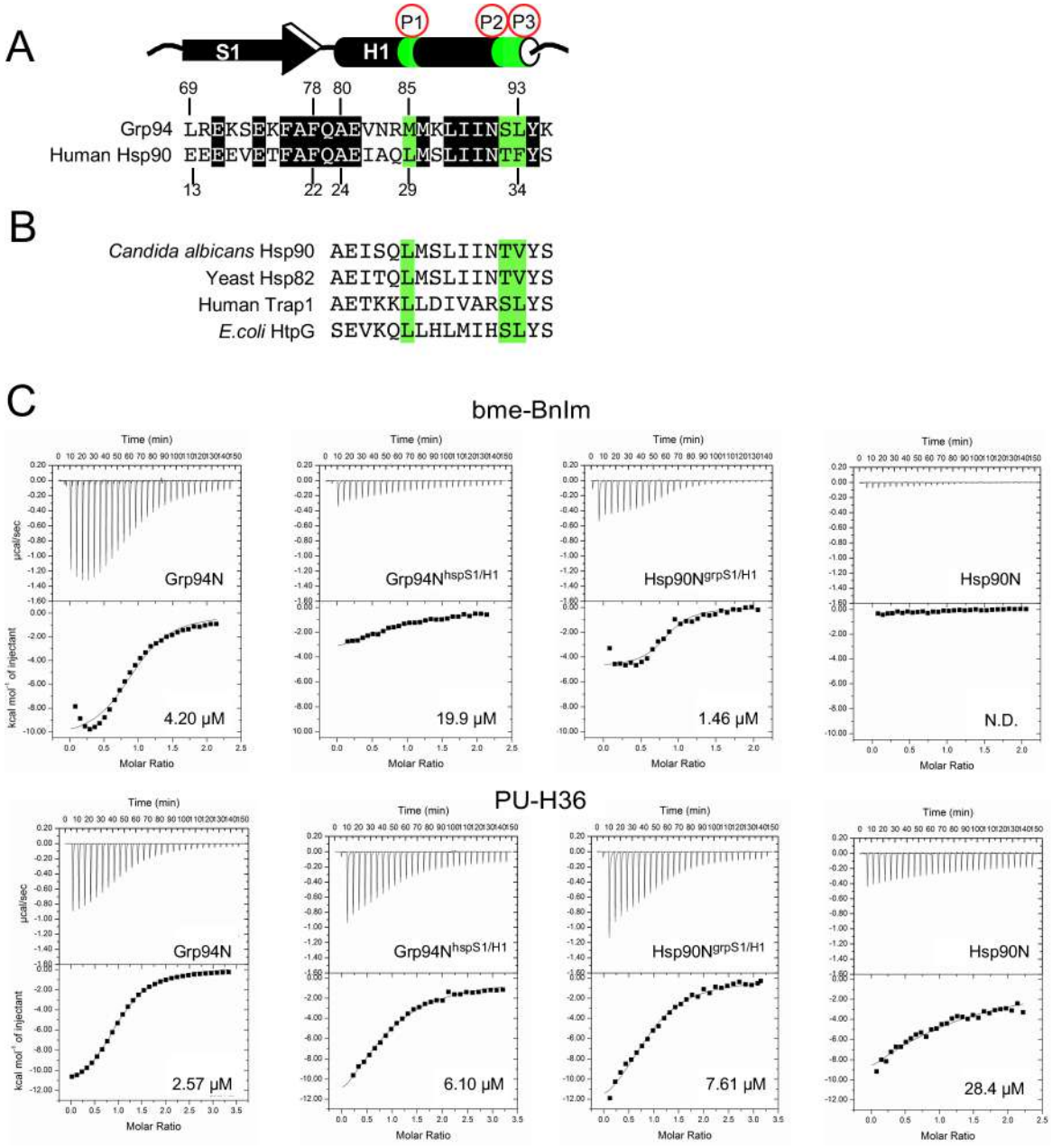

Figure 5. S1/H1 swaps confer Site 2 binding on Hsp90. (a) Comparison of S1 and H1 between Grp94 and Hsp90. Identical residues are shaded black, key discriminating residues in H1 are shaded green. (b) H1 residues for selected Hsp90 orthologs and paralogs. (c) ITC thermograms for the Site 2 binding, Grp94 selective ligands bme-BnIm and PU-H36. Thermograms for Grp94, Hsp90, and the S1/H1 chimeras are shown. bme-BnIm thermograms for Grp94N and Hsp90N are from Ref. 19.

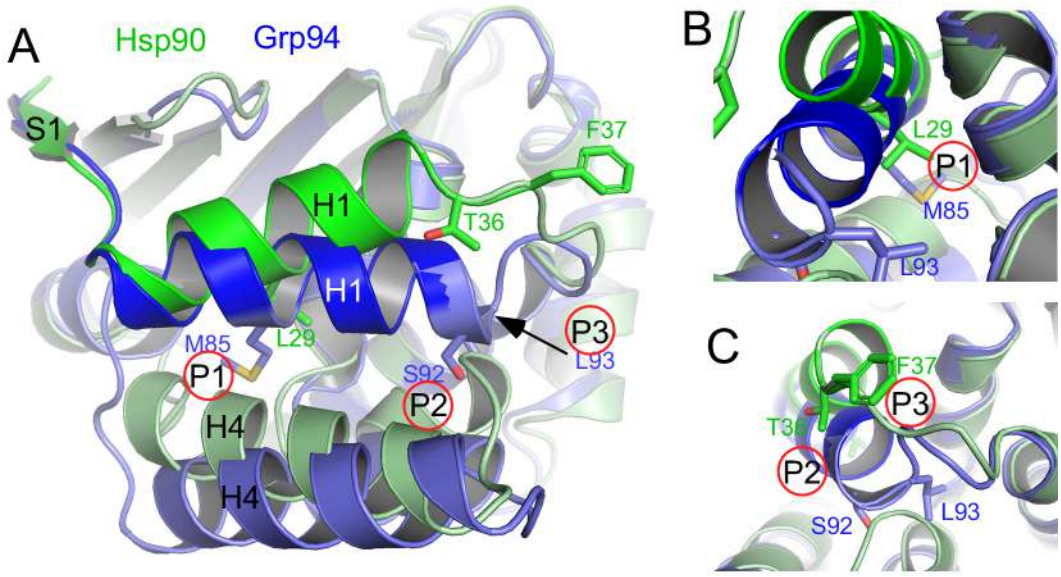

D

H1	H1 position	NTD body	H1/NTD Clashes	
Hsp90	Grp94	Grp94	P1 P2 P3	Y200, I90 T188 S189, T188, I192
Hsp90	Hsp90	Grp94	P1 P2 P3	none none none
Grp94	Hsp90	Hsp90	P1 P2 P3	T115, F118, M119 none none
Grp94	Grp94	Hsp90	P1 P2 P3	T185, V136, A111 I128, L122 I43, I128

Figure 6. H1 from Hsp90 and Grp94 differ. (a) Overlay of apo Hsp90 and apo Grp94. Hsp90 is colored green, Grp94 is colored blue. (b) Comparison of the positions of L29 and M85. (c) Comparison of the positions of F37 and L93. (d) Summary of modeled interactions in chimeric constructs.

Table 1. Thermodynamic parameters of binding

Protein	Ligand	K_d (μM)	N	ΔH (kcal/mol)	TΔS (kcal/mol)	ΔG (kcal/mol)
Grp94NΔ41[a]	bme-BnIm	4.2 ± 0.22	0.95 ± 0.00	-10.96 ± 0.07	-2.52 ± 0.09	-7.35 ± 0.03
$Grp94^{hspS1/H1}$	bme-BnIm	19.9 ± 1.59	1.2 ± 0.16	-5.75 ± 0.49	0.66 ± 0.54	-6.41 ± 0.05
$Hsp90^{grpS1/H1}$	bme-BnIm	1.3 ± 0.26	0.84 ± 0.01	-5.05 ± 0.33	2.99 ± 0.45	-8.04 ± 0.12
Hsp90N[a]	bme-BnIm	N.D.				
Grp94NΔ41	PU-H36	2.6 ± 0.05	0.98 ± 0.02	-11.92 ± 0.18	-4.28 ± 0.19	-7.64 ± 0.01
$Grp94^{hspS1/H1}$	PU-H36	6.1 ± 0.50	1.1 ± 0.06	-11.45 ± 0.16	-4.32 ± 0.13	-7.12 ± 0.04
$Hsp90^{grpS1/H1}$	PU-H36	7.6 ± 0.93	1.1 ± 0.04	-13.93 ± 0.59	-6.93 ± 0.74	-7.00 ± 0.14
Hsp90N	PU-H36	28.4 ± 3.3	1.0 ± 0.0	-23.78 ± 1.42	-17.58	-6.2
Hsp90N[b]	PU-H36	25.1 ± 4.0	1.9 ± 0.26	-8.31 ± 0.67	-2.03 ± 0.57	-6.28 ± 0.10
Grp94NΔ41	PU-H54	67 ± 9	1.3 ± 0.07	-5.66 ± 0.13	0.03	-5.69 ± 0.07
Hsp90N	PU-H54	225 ± 34	1.0 ± 0.0	-1.96 ± 0.18	3.0	-4.97 ± 0.08
Grp94NΔ41	PU-H71	0.049 ± 0.004	0.92 ± 0.01	-17.68 ± 0.04	-7.69 ± 0.08	-9.99 ± 0.05
$Grp94^{hspS1/H1}$	PU-H71	0.027 ± 0.003	0.95 ± 0.10	-12.34 ± 0.96	-2.02 ± 1.03	-10.32 ± 0.07
$Hsp90^{grpS1/H1}$	PU-H71	0.0037 ± 0.0007	0.94 ± 0.06	-12.81 ± 0.45	-1.46 ± 0.21	-11.43 ± 0.24
Hsp90N	PU-H71	0.0053 ± 0.0034	1.0 ± 0.02	-10.68 ± 0.30	0.69 ± 0.72	-11.36 ± 0.41
Grp94NΔ41	Radicicol	0.0015 ± 0.0007	1.1 ± 0.01	-22.50 ± 4.04	-10.42 ± 4.32	-12.08 ± 0.28
$Grp94^{hspS1/H1}$	Radicicol	0.0030 ± 0.0004	1.1 ± 0.02	-11.76 ± 0.52	-0.13 ± 0.60	-11.63 ± 0.07
$Hsp90^{grpS1/H1}$	Radicicol	0.0021 ± 0.0001	0.95 ± 0.07	-13.40 ± 1.42	-1.53 ± 1.13	-11.87 ± 0.29
Hsp90N	Radicicol	0.0004 ± 0.0001	0.94 ± 0.00	-22.98 ± 0.11	-10.19 ± 0.00	-12.79 ± 0.11

[a]Data from Ref. 19
[b]Data fit to a two site model

Table 2 – Data collection and Refinement Statistics

	hHsp90α:**PU-H36**	Grp94N:**PU-H36**	Grp94N:**PU-H71**
PDB code	8SBT	8TF0	8SSV
Source	SSRL 9-2	SSRL 9-2	APS 23ID-B
Space group	I 2 2 2	P 2_1 2_1 2_1	P 2_1
Unit cell: a, b, c, (Å);	66.61, 90.66, 98.48	96.28, 104.39, 172.28	51.90, 65.43, 75.38
Angles α, β, γ	90, 90, 90	90, 90, 90	90, 95.20, 90
Resolution (Å)	50.00-1.50	50.00-2.80	75.07-1.72
Last shell (Å)	1.55-1.50	2.90-2.80	1.93-1.72
Total (Unique) reflections	347,644 (91,288)	276,695 (43,634)	125,702 (23,864)
Completeness (last shell) (%)	99.9 (100.0)	99.9 (100.0)	91.3 (66.6) (ellipsoidal) 44.4 (7.5) (spherical)
Average I/σ_I (last shell)	48.31 (2.30)	22.77 (1.57)	8.9 (1.8)
Redundancy	3.8	6.3	5.3
R_{sym} (last shell)	0.040 (0.819)	0.107 (0.841)	0.106 (0.821)
R_{meas} (last shell)			0.118 (0.915)
R_{im} (last shell)		0.107 (0.841)	0.051 (0.396)
CC1/2 (last shell)	n/d	n/d	0.997 (0.655)
Refinement			
Resolution range (Å)	33.35-1.50	35.85- 2.80	75.07-1.72
Reflections	47,416	43,495	23,857
Non-solvent atoms (no H)	1,768	6,698	3,099
Solvent and heteroatoms	387	166	310
RMSD Bond lengths (Å)	0.016	0.002	0.006
RMSD Bond angles (°)	1.469	0.50	0.915
R_{work} (%)	0.1732	0.228	0.209
R_{free} (%)	0.1965	0.260	0.252
Structure solution	MR	MR	MR
All atom clashscore (B < 40)	3.34	6.25	5.01
Ramachandran favored (outlier) (%)	97.1 (0.0)	95.1 (0.35)	95.5 (0.0)
Overall score	1.28	1.70	1.58